HHS Public Access

Author manuscript

Physiol Meas. Author manuscript; available in PMC 2024 July 25.

Published in final edited form as:

Physiol Meas. ; 44(4): . doi:10.1088/1361-6579/acc780.

Reduced-order modeling and analysis of dynamic cerebral autoregulation via diffusion maps

K R M dos Santos[1,5], **M I Katsidoniotaki**[2,5,*], **E C Miller**[3], **N H Petersen**[4], **R S Marshall**[3], **I A Kougioumtzoglou**[2]

[1]Department of Civil, Environmental, and Geo- Engineering, University of Minnesota, Minneapolis, MN, United States of America

[2]Department of Civil Engineering and Engineering Mechanics, Columbia University, New York, NY, United States of America

[3]Neurology-Stroke Division, Neurological Institute of New York, Columbia University Medical Center, New York, NY, United States of America

[4]Department of Neurology, Yale University School of Medicine, New Haven, CT, United States of America

Abstract

Objective.—A data-driven technique for parsimonious modeling and analysis of dynamic cerebral autoregulation (DCA) is developed based on the concept of diffusion maps. Specifically, first, a state-space description of DCA dynamics is considered based on arterial blood pressure, cerebral blood flow velocity, and their time derivatives. Next, an eigenvalue analysis of the Markov matrix of a random walk on a graph over the dataset domain yields a low-dimensional representation of the intrinsic dynamics. Further dimension reduction is made possible by accounting only for the two most significant eigenvalues. The value of their ratio indicates whether the underlying system is governed by active or hypoactive dynamics, indicating healthy or impaired DCA function, respectively. We assessed the reliability of the technique by considering healthy individuals and patients with unilateral internal carotid artery (ICA) stenosis or occlusion. We computed the sensitivity of the technique to detect the presumed side-to-side difference in the DCA function of the second group (assuming hypoactive dynamics on the occluded or stenotic side), using McNemar's chi square test. The results were compared with transfer function analysis (TFA). The performance of the two methods was also compared under the assumption of missing data.

Main results.—Both diffusion maps and TFA suggested a physiological side-to-side difference in the DCA of ICA stenosis or occlusion patients with a sensitivity of 81% and 71%, respectively. Further, both two methods suggested the difference between the occluded or stenotic side and

*Author to whom any correspondence should be addressed. mk4121@columbia.edu.

[5]Equal contribution of authors.

Ethical statement

The research was conducted in accordance with the principles embodied in the Declaration of Helsinki and in accordance with local statutory requirements. All participants (all aged above 18) gave written informed consent to participate in the study. The IRB was the Columbia University Irving Medical Center (CUIMC) with protocol number is: AAAJ7502, currently active for analysis.

any two sides of the healthy group. However, the diffusion maps captured additional difference between the unoccluded side and the healthy group, that TFA did not. Furthermore, compared to TFA, diffusion maps exhibited superior performance when subject to missing data.

Significance.—The eigenvalues ratio derived using the diffusion maps technique can be potentially used as a reliable and robust biomarker for assessing how active the intrinsic dynamics of the autoregulation is and for indicating healthy versus impaired DCA function.

Keywords

cerebral autoregulation; cerebral hemodynamics; diffusion maps; mathematical modeling

1. Introduction

The term ‘dynamic cerebral autoregulation’ (DCA) refers to the ability of the cerebral vasculature to regulate cerebral blood flow in response to rapid changes in blood pressure. DCA is impaired in several neurological disorders (Donnelly *et al* 2015, Marshall *et al* 2016). Its dysfunction is associated with delayed cerebral ischemia after subarachnoid hemorrhage (Budohoski *et al* 2012), poor neurological outcomes in patients with traumatic brain injury (Rangel-Castilla *et al* 2008), and development of dementia in patients with mild cognitive impairment (Tarumi *et al* 2014). Devising precise and accurate techniques for DCA analysis, monitoring, and control is of importance to patient care, as it may allow for targeted and personalized management of blood pressure in patients with acute neurological illness (Petersen *et al* 2019).

Diverse techniques have been developed to assess and quantify DCA performance; see Czosnyka *et al* (2009) and Liu *et al* (2020) for some indicative reviews. Several of these techniques use continuous monitoring of arterial blood pressure (ABP) and cerebral blood flow velocity (CBFV), typically measured by transcranial Doppler. The methods aim to determine the extent to which changes in ABP correlate with changes in CBFV and, as a by-product, identify potentially impaired DCA function. Adopting a signals and systems terminology (Mitra 2016), a popular modeling approach considers an input–output relationship between ABP and CBFV to be identified. Additional input variables, such as the level of CO_2 (Kouchakpour *et al* 2010), have been used to more accurately model the input–output relationship. Regarding measurement methods, alternatives to transcranial Doppler include near-infrared spectroscopy (NIRS); see Fantini *et al* (2016) for a broad perspective.

The identified ABP-CBFV (input–output) functional relationship can be used as a diagnostic tool to inform clinicians of a patient’s state relative to the limits of autoregulatory function. A broad range of methodologies has been developed in the literature with varying degrees of success for modeling and, ultimately, quantifying DCA performance. For example, the widely used method of transfer function analysis (TFA) (Blaber *et al* 1997, Claassen *et al* 2016) employs estimates of the auto- and cross-spectra of ABP and CBFV to determine the relationship between ABP (input) and CBFV (output). These auto- and cross-spectra estimates are used to obtain the phase shift, which quantifies the time-lag of the output signal compared to the input and is used for assessing the DCA performance. The TFA method assumes inherently not only a linear but also a time-invariant system and treats the

measured data as stationary (i.e. with time-invariant statistics). However, most measured CBFV and ABP time-histories are transient, aperiodic, and intermittent by nature, and demonstrate non-stationary behavior (Marmarelis *et al* 2014, Panerai 2014), particularly in the presence of variations in CO_2 (Liu *et al* 2010, Kostoglou *et al* 2014). In this regard, traditional time-invariant signal processing techniques, such as Fourier transform analysis used in TFA, are unable to capture the time-variant frequency content of the system dynamics.

Alternative methods capable of performing joint time-frequency analyses (Tian *et al* 2016, Chalak and Zhang 2017, Aleksandrin *et al* 2018) employ wavelet families (e.g. Morlet wavelet) requiring, typically, two parameters for their definition, characterizing the scale and the translation level (Mallat 1999, Latka *et al* 2005, Addison 2015). Recent work by Miller *et al* (2020) used another alternative—a joint time-frequency analysis technique based on generalized harmonic wavelets (GHWs) for DCA performance quantification. In comparison to existing wavelet-based techniques available in the literature that employ standard dyadic decompositions (Addison 2015), the advantage of GHWs is that they possess an additional coefficient which decouples the wavelet resolution in the frequency domain from the central frequency of the wavelet allowing enhanced resolution in frequency regions of interest. However, although the GHW-based methodology can account for the temporal dynamics of the DCA function, its validity remains restricted to cases satisfying the assumption of linear relationship between input–output (ABP-CBFV) data.

To account for nonlinear system modeling in the input–output relationship between ABP and CBFV, other methodologies have been proposed, such as the ones based on Volterra–Wiener representations of nonlinear systems (Panerai *et al* 1999, Kouchakpour *et al* 2010); see also Schetzen (2006) for a broad perspective. However, the success of such methodologies, especially for real-time analysis and diagnostics, is hindered by the significant computational cost related to the numerical integration of multi-convolution integrals. The time correlation method yields a coefficient quantifying the correlation degree between ABP and CBFV (Liu *et al* 2020). Positive values indicate impaired autoregulation, whereas zero or negative values imply intact autoregulation. Although this method has proved to be a relatively reliable instantaneous descriptor of autoregulation, it provides no information about the underlying governing DCA dynamics and no insight regarding the autoregulation mechanism.

In recent years, a novel paradigm of data-driven model discovery has emerged (Bongard and Lipson 2007, Brunton and Kutz 2019) employing machine learning approaches, such as neural networks and various regression schemes, for modeling time-series data in a broad range of scientific disciplines (Vlachas *et al* 2018, Raissi *et al* 2019, Zhu *et al* 2019). This framework can readily account for arbitrary nonlinear and time-variant behaviors, and is driven by the fact that in many problems, particularly physiological mechanisms, purely physics-based, first-principles based the modeling of the governing dynamics may be untenable. Research efforts toward data-driven DCA modeling and analysis include work by Tan (2012), where a projection pursuit regression scheme was employed, and by Panerai *et al* (2004) and Al-Abed *et al* (2019), where extrapolation approaches based on artificial neural networks were proposed. However, for data-driven modeling to be effective,

the identified model should exhibit sparsity in the sense that the fewest possible terms are considered for the description of the system dynamics. This approach enhances the interpretability of the model, and provides balance between model complexity and accuracy. The rationale for such data-driven discovery of governing equations and identification of parsimonious system dynamics relates to the fact that the dynamics of most physical systems, including physiological mechanisms, can be described accurately by considering only a few relevant terms in an appropriate expansion basis, thus rendering the governing equations sparse in a high-dimensional nonlinear function space.

Here, we develop a data-driven technique for parsimonious modeling and analysis of DCA by relying on the concept of diffusion maps (Coifman and Lafon 2006, Nadler *et al* 2006). Specifically, the strong and restrictive assumption of an input–output relationship between ABP and CBFV is circumvented. A more general state-space description of DCA dynamics based on variables ABP, CBFV, and their time derivatives is considered, yielding a low-dimensional representation of the intrinsic dynamics. This is accomplished by performing an eigendecomposition of the Markov matrix of a random walk on a graph constructed over the dataset domain. The obtained eigenvectors and eigenvalues determine a new coordinate set embedding the high-dimensional information into a low-dimensional space (Coifman *et al* 2008, Singer *et al* 2009). Further dimension reduction is possible by accounting only for the two most significant eigenvalues (Dsilva *et al* 2018). The value of their ratio indicates whether active or hypoactive dynamics govern the underlying system. This ratio has the potential to be used as a clinical biomarker for diagnosing healthy versus impaired DCA function. We aimed to demonstrate the efficacy of this approach by considering healthy individuals and patients with unilateral internal carotid artery (ICA) stenosis or occlusion whose DCA function is presumed to be poorer on the stenotic or occluded side (Reinhard *et al* 2003b).

2. Materials and methods

2.1. Subjects

Two groups of volunteers were considered to assess the performance of the developed technique: 46 healthy people under 60 years of age (19 men and 27 women), and 31 patients with unilateral ICA stenosis or occlusion (80%–100% occlusion) without stroke history (22 men and 9 women). In the second group, 14 (45%) had a completely occluded ICA, and 17 (55%) had 80%–99% stenosis. ICA stenosis >70% is associated with impaired DCA (Reinhard *et al* 2003a). We used this known asymmetry of the stenosis/occlusion in the two sides of the brain to demonstrate the sensitivity of the technique.

2.2. Data acquisition and processing

Participants' data were collected at Columbia University Irving Medical Center (CUIMC) from August 2011 to January 2019. All volunteers provided written informed consent. Unilateral ICA stenosis or occlusion was confirmed by carotid duplex Doppler, computed tomographic angiography, or magnetic resonance angiography. The study protocol was approved by the Institutional Review Board of CUIMC.

During the data acquisition process, the participants lay supine wearing a head frame connected with a 2 MHz transcranial Doppler probe and a properly-sized finger cuff attached with servo-controlled in-phase finger plethysmography (Finometer Pro, Amsterdam, Netherlands). Transcranial Doppler was used to measure the CBFV by insonating the left and right proximal cerebral arteries at a depth of 45–60 mm. The plethysmography measured the ABP non-invasively. ABP and CBFV signals were recorded for 10 min at 100 Hz. Both ABP and CBFV signals were filtered with a band-pass filter in the frequency range [0.01–0.13] Hz (Fantini *et al* 2016.

2.3. Mathematical aspects of diffusion maps and reduced-order modeling of DCA dynamics

Data obtained by observing the evolution in time of a dynamic system can be succinctly represented in many cases in low-dimensional domains, providing insights about the intrinsic dynamics, and facilitating the interpretation of complex phenomena (Roweis and Saul 2000, Tenenbaum *et al* 2000, Donoho and Grimes 2003, Dos Santos *et al* 2022). The current analysis made use of the concept of diffusion maps (Nadler *et al* 2006, Coifman *et al* 2008, Singer *et al* 2009, Dsilva *et al* 2018). This technique relies on an eigendecomposition of the transition probability of a random walk on a graph constructed over the dataset. The obtained eigenvectors and eigenvalues are associated with a new coordinate set embedding the high-dimensional information into a low-dimensional space. An efficacious representation of the resulting lower-dimensional model considers the two most important eigenvectors only.

2.3.1. Reduced-order modeling—DCA is typically modeled by relying on an input–output relationship of the form $v = \mathcal{M}(p)$; where $p = \text{ABP}, v = \text{CBFV}$, and $\mathcal{M}(\cdot)$ represents the mathematical model to be identified relating the input p to the output v. An alternative modeling approach that does not assign *a priori* the roles of an input and an output to p and v, respectively, offers more versatility. Here, p, v, and their respective time derivatives, $\dot{p}$ and $\dot{v}$, are considered to describe the observed state of the DCA model in a four-dimensional space. Consider a dataset $S = \{\mathbf{x}_1, \ldots, \mathbf{x}_N\}$ comprising N discrete observations of the DCA state $\mathbf{x}_i = [v_i, p_i, \dot{v}_i, \dot{p}_i]^T$. A fully connected graph is constructed over this dataset where the nodes are the observed state $\mathbf{x}_i = [v_i, p_i, \dot{v}_i, \dot{p}_i]^T$, and the edges have weights given by the pairwise similarity of the elements in S determined by the Gaussian kernel

$$k(\mathbf{x}_i, \mathbf{x}_j) = \exp\left(-\frac{\| \mathbf{x}_i - \mathbf{x}_j \|_2^2}{\varepsilon^2}\right). \tag{1}$$

In equation (1) $\| \mathbf{x}_i - \mathbf{x}_j \|_2$ is the Euclidean distance between $\mathbf{x}_i$ and $\mathbf{x}_j$, and ε is a length-scale parameter, estimated as the median of the pairwise distance of the points in S. The transition probabilities $M_{ij} = P(\mathbf{x}_j \mid \mathbf{x}_i)$ of the Markov matrix $\mathbf{M} \in \mathbb{R}^{N \times N}$ are constructed as

$$M_{ij} = \frac{k^{\star}_{ij}}{\sum_{k=1}^{N} k^{\star}_{ik}}, \tag{2}$$

where $D_{ii} = \sum_{j=1}^{N} k_{ij}$ and $k^{\star}_{ij} = k_{ij}/\sqrt{D_{ii}D_{jj}}$. In Eq.(2) the notation $k(\mathbf{x}_i, \mathbf{x}_j) = k_{ij}$ is used for simplicity. According to the diffusion maps theory, the reduction of the high-dimensional system into a low-dimensional Euclidean space is performed by determining a new coordinate system $\xi(\mathbf{x}_i) = [\lambda_1\psi_1(i), \ldots, \lambda_N\psi_N(i)]$, where $\Psi = [\psi_1, \ldots, \psi_N]$ and $(\lambda_1, \ldots, \lambda_N)$ are the eigenvectors and eigenvalues of $\mathbf{M}$, respectively. Note that only the eigenvectors associated with significant eigenvalues, i.e. $\sum_{i=1}^{q} \lambda_i \geqslant 0.95 \cdot \sum_{j=1}^{N} \lambda_j$, are considered. This yields a subset of $q < N$ eigenvectors. Additional reduction of this subset is possible by identifying only those eigenvectors that are linearly independent. This is done by employing a local linear regression scheme (Dsilva *et al* 2018). Specifically, a given eigenvector is expressed as a linear combination of the remaining eigenvectors, i.e.

$$\psi_k(i) \approx \alpha_k(i) + \beta_k^T(i)\mathbf{\Psi}_{k-1}(i), \tag{3}$$

where i is the entry index of ψ_k, $\mathbf{\Psi}_{k-1}\left(i\right) = [\psi_1(i), \ldots, \psi_{k-1}(i)]^T$, $\alpha_k\left(i\right) \in \mathbb{R}$, $\beta_k\left(i\right) \in \mathbb{R}^{k-1}$, and $k \leqslant q$. Next, the coefficients $\alpha_k(i)$ and $\beta_k(i)$ are determined by solving the optimization problem

$$\hat{\alpha}_k(i), \hat{\beta}_k(i) = \underset{\alpha, \beta}{\operatorname{argmin}} \sum_{j \neq i} k_{k-1}^{ij} \cdot \left(\psi_k(j) - \alpha_k + \beta_k^T \mathbf{\Psi}_{k-1}(j)\right)^2, \tag{4}$$

where $k_{k-1}^{ij} = k(\mathbf{\Psi}_{k-1}(i), \mathbf{\Psi}_{k-1}(j))$ is computed using equation (1). Further, the residuals r_k are estimated by the normalized leave-one-out cross-validation error for the local linear fit, i.e.

$$r_k = \sqrt{\frac{\sum_{i=1}^{q} \left\{\psi_k(i) - \left[\hat{\alpha}_k(i) + \hat{\beta}_k^T(i)\mathbf{\Psi}_{k-1}(i)\right]\right\}^2}{\sum_{i=1}^{q} \psi_k^2(i)}}. \tag{5}$$

Large values of r_k correspond to eigenvectors that are linearly independent from the rest of the eigenvectors.

2.3.2. Proposing a biomarker for indicating healthy versus impaired DCA function—

Following Dsilva *et al* (2018), the ratio

$$\gamma = \sqrt{\frac{\log(\lambda_1^{\star})}{\log(\lambda_2^{\star})}}$$

(6)

can approximately determine the effective dimensionality of the underlying dynamic system, where $\lambda_1^\star$ and $\lambda_2^\star$ denote the two leading eigenvalues corresponding to unique eigen-directions. In fact, γ can be potentially used as a metric for assessing the dynamic behavior of cerebral autoregulation. Specifically, for $\gamma \to 0$ the data become 1-dimensional since only one eigendirection is most dominant, whereas for $\gamma \to 1$ the data become 2-dimensional indicating more active dynamics. Therefore, we conjecture that $0 \leqslant \gamma \leqslant 1$ can to classify the DCA function into healthy (i.e. more active dynamics as $\gamma \to 1$) and impaired (i.e. less active dynamics as $\gamma \to 0$).

2.3.3. Mechanization of the technique—The mechanization of the proposed technique based on diffusion maps for DCA parsimonious modeling and analysis comprises the following steps (see also figure 1):

1. ABP and CBFV time-histories corresponding to both sides of the brain are acquired and a band-pass filter is applied to extract only the low-frequency content in the range [0.01,0.13] Hz.
2. The Gaussian kernel is determined using equation (1) for a random sample of states.
3. The Markov matrix **M** is estimated using equation (2), and its eigenvalues and eigenvectors are computed.
4. The parsimonious representation of the underlying dynamics is determined by selecting only $k \leqslant q < N$ eigenvalues based on the local linear regression scheme and the magnitude of the residuals in equation (3).
5. Compute the dimensionality ratio γ using equation (6).
6. If the dimensionality ratio $\gamma \to 0$ and, equivalently, a single diffusion coordinate $\lambda_k^\star \cdot \psi_k(i)$ is dominant, figure 1 (top right), the system exhibits hypoactive dynamics indicating a potentially impaired DCA function. If the dimensionality ratio $\gamma \to 1$, the system exhibits more active dynamics, considered to be indicative of a healthier DCA function (bottom right).

2.4. Statistical analysis

The reliability of the developed technique for identifying impaired DCA is assessed by considering two groups of volunteers (healthy and unilateral ICA stenosis or occlusion patients). The statistical analysis of γ includes the estimation of the median and the interquartile range (IQR) for both healthy and ICA stenosis or occlusion volunteers. We compared the medians of the two sides within the same group (left versus right cerebral hemispheres for the healthy individuals, and occluded/stenotic versus unoccluded side of the brain for the ICA stenosis or occlusion patients). In addition, we compared median values between 3 groups: cerebral hemispheres in the territory of occluded or stenotic carotid arteries; hemispheres in the territory of unoccluded carotid arteries in participants with unilateral ICA stenosis or occlusion, and hemispheres in the territory of the healthy

(unoccluded) carotid arteries. Medians were compared between groups using the Kruskal–Wallis test with an alpha level of 5%.

We then compared standard TFA (Claassen *et al* 2016) with the diffusion maps technique. Median phase shift was calculated for the aforementioned groups. We compared the sensitivity of the two techniques to accurately differentiate occluded/stenotic from unoccluded sides using the McNemar's chi square test (Trajman and Luiz 2008, Kim and Lee 2017), with an alpha level of 5%. TFA was considered to successfully identify impaired autoregulation if the phase shift of the occluded/stenotic side was lower compared to the unoccluded side (Reinhard *et al* 2003b). The diffusion maps technique was considered to detect the occluded/stenotic side if the γ was lower compared to the unoccluded side.

Lastly, the effect of the number N of the randomly selected samples on estimating the dimensionality ratio γ was investigated. In figure 2, the mean and the standard deviation of the estimated dimensionality ratio γ are plotted as a function of N for a randomly selected healthy volunteer and a randomly selected patient with carotid stenosis/occlusion. Note that the length of the recorded signals is 55 000. The process is repeated 20 times for each volunteer. It is seen that the variability in the estimates reaches a minimum at 3000 samples, approximately, and does not decrease further with larger sample numbers. Therefore, in the ensuing analysis, the value $N = 3000$ is used.

3. Results

3.1. Application to synthetic data

The dimensionality ratio γ is obtained for an example considering synthetic data, simulating one side of the brain as occluded, i.e.

$$\begin{aligned}\mathrm{ABP} &= \cos(2\pi 2t) + 2\cos(2\pi 0.1t) + 3\cos(2\pi 0.05t)\\ \mathrm{CBF}_1 &= \cos(2\pi 2t - \phi_1) + 2\cos(2\pi 0.1t - \phi_1) + 3\cos(2\pi 0.05t - \phi_1)\\ \mathrm{CBF}_2 &= \cos(2\pi 2t - \phi_2) + 2\cos(2\pi 0.1t - \phi_2) + 3\cos(2\pi 0.05t - \phi_2),\end{aligned} \tag{7}$$

where $\phi_1 = \pi/12t^{0.1}$ and $\phi_2 = \pi/6t^{0.1}$ are the time-dependent phase shifts of CBF_1 and CBF_2, respectively, that simulate the blood flow in the two sides of the brain. The blood flow with the smallest phase shift, i.e. CBF_1, corresponds to the occluded side of the brain, since the flow is less efficient to counter-regulate the pressure, whereas the largest phase shift corresponds to the unoccluded side (Marshall *et al* 2016). Further, the synthetic ABP-CBF signals in equation (7) are discretized into 55 000 time points, simulating the actual length of the recorded signals.

First, the signals are filtered (figure 3) with a band-pass filter in the frequency range [0.01–0.13] Hz, which is equivalent to deleting the first cosine term of frequency 2 Hz in each signal. According to the diffusion maps technique, $N = 3000$ samples are randomly selected from each signal. Next, following the eigendecomposition of the estimated Markov matrix $\mathbf{M}$ and the parsimonious representation of each side of the brain, the selected

eigenvalues $\lambda_1^\star, \lambda_2^\star$ corresponding to the largest residual values yield the dimensionality ratios $\gamma_1 = \sqrt{\frac{\log(\lambda_1^*)}{\log(\lambda_2^*)}} = 0.66$ and $\gamma_2 = \sqrt{\frac{\log(\lambda_1^*)}{\log(\lambda_2^*)}} = 0.90$. Therefore, as anticipated based on the constructed signals and according to the rationale developed in section 2.3.2, smaller values of γ indicate lower-dimensional, hypoactive, dynamics corresponding to impaired DCA function, whereas larger values of γ indicate higher-dimensional, active, dynamics corresponding to healthy DCA function.

3.2. Eigenvalue analysis for an indicative patient

The dimensionality ratio γ is obtained for an indicative ICA stenosis patient with the left side of the brain occluded. Specifically, an ensemble of signals comprising 10 minutes of ABP-CBFV time-histories are considered discretized into 55 000 time points, out of which only 3000 samples are randomly selected (figure 4). Next, following the eigendecomposition of the estimated Markov matrix **M**, the $q = 5$ largest eigenvalues are plotted in figure 5 referring to the occluded side (top), and to the unoccluded side (bottom). Higher color intensity indicates larger residual values calculated by equation (6). For the occluded side, the 1st and the 4th eigenvalues correspond to the largest residual values yielding a ratio $\gamma = 0.65$, whereas for the unoccluded side the 1st and the 2nd eigenvalues correspond to the largest residual values yielding a ratio $\gamma = 0.86$. Further, the diffusion coordinates $\lambda_k^\star \cdot \psi_k(i)$ of the largest residual values are plotted in figure 6, where for the occluded side it is seen that one coordinate is significantly more dominant than the other. Therefore, based on the rationale developed in section 2.3.2, smaller values of γ indicate lower-dimensional, hypoactive, dynamics corresponding to impaired DCA function, whereas larger values of γ indicate higher-dimensional, active, dynamics corresponding to healthy DCA function.

3.3. Healthy volunteers

Among healthy volunteers, the median (IQR) of the dimensionality ratio γ was 0.78 (0.71–0.84) for the left side and 0.76 (0.67–0.83) for the right side, as shown in figure 7 and table 1 with no significant between-group difference ($p = 0.47$).

3.4. Carotid stenosis or occlusion volunteers

Among all participants with unilateral ICA stenosis or occlusion, the median (IQR) of the dimensionality ratio γ was 0.62 (0.54–0.74) for the occluded/stenotic side and 0.66 (0.58–0.77) for the unoccluded side, as shown in figure 7 and table 1 ($p = 0.05$). The dimensionality ratio for each side in the carotid stenosis or occlusion subjects was significantly lower than healthy controls ($p = 10^{-5}$ for the occluded/stenotic versus healthy controls and $p = 0.005$ for the unoccluded side versus healthy controls) suggesting significant physiological differences between the unoccluded side of ICA stenosis or occlusion patients and any of the two sides of healthy patients.

3.5. Comparison with standard TFA

Among healthy subjects, median (IQR) phase shift was 41.0(31.8–52.2) and 46.3(33.6–55.2) degrees for the left and the right sides, respectively ($p = 0.61$) as shown in figure 8 and table

2. Among unilateral ICA stenosis or occlusion participants, median (IQR) phase shift was 28.8(19.5–42.9) degrees for the occluded/stenotic side and 42.7(30.6–50.8) degrees for the unoccluded side ($p < 0.05$). Similar results were found in Reinhard *et al* (2003a). Comparing each side of the ICA stenosis or occlusion participants with the healthy participants, TFA estimates did not suggest impairment of the unoccluded side.

3.6. Sensitivity and specificity comparison of the two techniques

The sensitivity of the diffusion maps technique to correctly identify the occluded/stenotic from the unoccluded side was 25 out of the 31 (81%) by comparing γ for both sides of the brain. The TFA method correctly identified 22 out of the 31 occluded/stenotic sides (71%) by comparing phase shifts for both sides of the brain. According to the McNemar's test, the chi-squared is equal to 0.8 and the $p = 0.36 > 0.05$, when comparing γ with phase shifts.

The specificity of the diffusion maps technique to correctly identify the sides of the brain as healthy was 43 out of the 46 (93%) by comparing γ for both sides of the brain with a 10% margin of error. The TFA method specificity to correctly identify the sides of the brain as healthy was 31 out of the 46 (71%) by comparing phase shifts for both sides of the brain with a 10% margin of error. According to the McNemar's test, the chi-squared is equal to 9 and the $p = 0.003 < 0.05$, when comparing γ with phase shifts.

3.7. Robustness of the technique subject to missing data

The diffusion maps technique does not require any information regarding the position of the measured data in time. The considered dataset is selected randomly and constitutes a small subset of the total measured data. This provides flexibility in avoiding time intervals with incomplete data or areas in the time domain with apparent artifacts. This is not the case with a TFA treatment, where the time sequence of the data points matters and needs to be accounted for. We anticipated that the diffusion map technique would exhibit superior performance and provide more robust estimates compared to TFA when subject to missing data.

To support the above argument, a numerical example is considered. First, three blocks of missing data of varying length are considered in the measured CBFV signals, whereas the length of the blocks is expressed as a percentage of missing data over the total length of the signal, i.e. 55 000 samples; see also figure 9 for an indicative illustration. Second, the missing data are replaced with the mean value of the signal and a band-pass filter is applied to extract only the low-frequency content in the range [0.01, 0.13] Hz. Lastly, the process is repeated for 20 randomly selected healthy patients and estimates of the dimensionality ratio γ are obtained based on diffusion maps, and estimates of the phase shift are obtained based on TFA. The average relative errors based on comparisons with analyses using the complete set of data are shown in figure 10. The TFA-based estimates were considerably affected by the missing data. Even for a relatively small percentage of missing data (e.g. 5%), the error in estimating the phase shift approached 7%. All 55 000 samples were used for the TFA analysis. In contrast, selecting randomly only 3000 samples, i.e. 5% of the total 55 000 samples for the diffusion maps analysis yielded γ estimates for which the corresponding error was not more than 2%–3% in the worst case scenario.

4. Discussion

In this paper, we developed a data-driven technique for reduced-order modeling and analysis of DCA based on the concept of diffusion maps. Specifically, we considered a state-space description of DCA dynamics based on variables ABP, CBFV, and their time derivatives, yielding a low-dimensional representation of the intrinsic dynamics. This was done by performing an eigendecomposition of the Markov matrix of a random walk on a graph constructed over the dataset domain. The obtained eigenvectors and eigenvalues determine a new coordinate set embedding the high-dimensional information into a low-dimensional space. Our results demonstrate that the ratio of the two most significant eigenvalues, i.e. the dimensionality ratio, successfully indicates active or hypoactive dynamics for each side of the brain. This method could be potentially employed as a diagnostic tool and a biomarker for indicating healthy versus impaired DCA function and successfully identifying side-to-side differences due to pathological conditions.

One advantage of the diffusion maps technique versus other techniques is its accuracy, since it realistically accounts for nonlinear and non-stationary relationships between ABP and CBFV data. In our analysis, diffusion maps captured impaired intrinsic dynamics even for the unoccluded side of carotid stenosis or occlusion patients, in contrast to the TFA which classifies them as unaffected. Such a finding is reasonable (Marshall *et al* 2017), due to additional pathological conditions that may exist in this clinical group, e.g. cerebral small vessel disease, that affects both sides of the brain.

Another important advantage of this technique is that diffusion maps require only a relatively small number of randomly selected points from the measured ABP and CBFV signals. This renders the process more robust in the case of missing data. The diffusion maps method exhibited smaller relative error under conditions of incomplete data in the signals since it does not rely on the sample sequence, in contrast with the TFA. This is particularly important in clinical measurements where missing data and noise are significant and as a result, a large amount of data may not be usable.

Additionally, diffusion maps exhibited a higher degree of accuracy in correctly classifying the two sides of the brain as occluded/stenotic and unoccluded compared to TFA. However, additional subjects are needed to support the statistical significance of the argument, as well as to define a more accurate range of the ratios corresponding to occluded/stenotic and unoccluded sides of the ICA patients. Lastly, limitations of our study relate to the fact that analysis of the direct agreement of the proposed technique with TFA in the healthy group is not feasible, e.g. Bland–Altman plots, since the two techniques have different metrics. Also, we did not account for continuous capnography during the data acquisition, and neither for hypercapnia to capture time-variant behavior. Yet we believe that the presented technique will be suitable for those cases since it accounts for non-stationarity in the signals.

Acknowledgments

This study was supported by the Columbia University School of Engineering and Applied Science Translational Acceleration Research Fund, the National Institutes of Health (NIH) National Institute for Neurological Disorders and Stroke (Grant No. K23NS107645 (ECM)), and the Louis V Gerstner Jr Foundation (Gerstner Scholars Program (ECM)).

Data availability statement

The data cannot be made publicly available upon publication because they contain sensitive personal information. The data that support the findings of this study are available upon reasonable request from the authors.

References

Addison PS 2015 A review of wavelet transform time-frequency methods for NIRS-based analysis of cerebral autoregulation IEEE Rev. Biomed. Eng 8 78–85 [PubMed: 26011892]

Al-Abed MA, Al-Bashir AK, Al-Rawashdeh A, Alex RM, Zhang R, Watenpaugh DE and Behbehani K 2019 Estimation of cerebral blood flow velocity during breath-hold challenge using artificial neural networks Comput. Biol. Med 103508 [PubMed: 31698237]

Aleksandrin VV, Ivanov AV, Virus ED, Bulgakova PO and Kubatiev AA 2018 Application of wavelet analysis to detect dysfunction in cerebral blood flow autoregulation during experimental hyperhomocysteinaemia Lasers Med. Sci 33 1327–33 [PubMed: 29611066]

Blaber AP, Bondar RL, Stein FT Dunphy P, Moradshahi P, Kassam MS and Freeman R 1997 Transfer function analysis of cerebral autoregulation dynamics in autonomic failure patients Stroke 28 1686–92 [PubMed: 9303010]

Bongard J and Lipson H 2007 Automated reverse engineering of nonlinear dynamical systems Proc. Natl. Acad. Sci 104 9943–8 [PubMed: 17553966]

Brunton SL and Kutz JL 2019 Data-driven Science and Engineering: Machine Learning, Dynamical Systems and Control (UK: Cambridge University Press)

Budohoski KP, Czosnyka M, Smielewski P, Varsos GV, Kasprowicz M, Brady KM, Pickard JD and Kirkpatrick PJ 2012 Cerebral autoregulation after subarachnoid hemorrhage: comparison of three methods J. Cerebral Blood Flow Metab 33 449–56

Chalak L and Zhang R 2017 New wavelet neurovascular bundle for bedside evaluation of cerebral autoregulation and neurovascular coupling in newborns with hypoxic-ischemic encephalopathy Developmental Neurosci. 39 89–96

Claassen JA, van den Abeelen ASM, Simpson DM and Panerai RB 2016 Transfer function analysis of dynamic cerebral autoregulation: a white paper from the international cerebral autoregulation research network J. Cerebral Blood Flow Metab 36 665–80

Coifman RR, Kevrekidis IG, Lafon S, Maggioni M and Nadler B 2008 Diffusion maps, redaction coordinates, and low dimensional representation of stochastic systems Multiscale Model. Simul 7 842–64

Coifman RR and Lafon S 2006 Diffusion maps Appl. Comput. Harmon. Anal 21 5–30

Czosnyka M, Brady K, Reinhard M, Smielewski P and Steiner LA 2009 Monitoring of cerebrovascular autoregulation: facts, myths, and missing links Neurocritical Care 10 373–86 [PubMed: 19127448]

Donnelly J, Aries MJ and Czosnyka M 2015 Further understanding of cerebral autoregulation at the bedside: possible implications for future therapy Expert Rev. Neurotherapeutics 15 169–85

Donoho DL and Grimes C 2003 Hessian eigenmaps: locally linear embedding techniques for high-dimensional data Proc. Natl Acad. Sci 100 5591–6 [PubMed: 16576753]

Dos Santos KRM, Giovanis DG and Shields MD 2022 Grassmannian diffusion maps based dimension reduction and classification for high-dimensional data SIAM Journal on Scientific Computing 44 B250–B274

Dsilva CJ, Talmon R, Coifman RR and Kevrekidis IG 2018 Parsimonious representation of nonlinear dynamical systems through manifold learning: a chemotaxis case study Applied and Computational Harmonic Analysis 44 759–773

Fantini S, Sassaroli A, Tgavalekos KT and Kornbluth J 2016 Cerebral blood flow and autoregulation: current measurement techniques and prospects for noninvasive optical methods Neurophotonics 3 031411 [PubMed: 27403447]

Kim S and Lee W 2017 Does mcnemar's test compare the sensitivities and specificities of two diagnostic tests? Stat. Methods Med. Res 26 142–54 [PubMed: 24996898]

Kostoglou K, Debert CT, J Poulin M and D Mitsis G 2014 Nonstationary multivariate modeling of cerebral autoregulation during hypercapnia Med. Eng. Phys 36 592–600 [PubMed: 24291338]

Kouchakpour H, Allen R and Simpson DM 2010 Nonlinear, multiple-input modeling of cerebral autoregulation using volterra kernel estimation 2010 Annual Int. Conf. of the IEEE Engineering in Medicine and Biology pp 2375–8

Latka M, Turalska M, Glaubic-Latka M, Kolodziej W, Latka D and J B 2005 Phase dynamics in cerebral autoregulation Am. J. Physiol. Heart Circ. Physiol 289 H2272–9 [PubMed: 16024579]

Liu J, Simpson MD, Yan J and Allen R 2010 Tracking time-varying cerebral autoregulation in response to changes in respiratory PaCO2 Physiol. Meas 31 1291–307 [PubMed: 20720290]

Liu X, Czosnyka M, Donelly J, Cardim D, Cabeleira M, Lalou DA, Hu X, Hutchinson PJ and Smielewski P 2020 Assessment of cerebral autoregulation indices-a modelling perspective Sci. Rep 10 9600 [PubMed: 32541858]

Mallat S 1999 A Wavelet Tour of Signal Processing (Burlington, MA: Elsevier Science)

Marmarelis VZ, Shin DC, Orme ME and Zhang R 2014 Time-varying modeling of cerebral hemodynamics IEEE Trans. Biomed. Eng 61 694–704 [PubMed: 24184697]

Marshall RS, Asllani I, Pavol MA, Slattery P and Lazar RM 2017 Regional hypoperfusion is associated with cortical thinning in asymptomatic carotid artery disease Int. Stroke Conf 2

Marshall RS, Pavol MA, Cheung YK, Strom I, Asllani I and Lazar RM 2016 Dissociation among hemodynamic measures in asymptomatic high grade carotid artery stenosis J. Neurol. Sci 367 143–7 [PubMed: 27423579]

Miller EC, Dos Santos KRM, Marshall RS and Kougioumtzoglou IA 2020 Joint time-frequency analysis of dynamic cerebral autoregulation using generalized harmonic wavelets Physiol. Meas 41 024002 [PubMed: 32000149]

Mitra S 2016 Signal and Systems (Oxford: Oxford University Press)

Nadler B, Lafon S, Coifman RR and Kevrekidis IG 2006 Diffusion maps, spectral clustering and reaction coordinate of dynamical systems Appl. Comput. Harmon. Anal 21 113–27

Panerai R, Chacon M, Pereira R and Evans D 2004 Neural network modelling of dynamic cerebral autoregulation: assessment and comparison with established methods Med. Eng. Phys 26 43–52 [PubMed: 14644597]

Panerai RB 2014 Nonstationarity of dynamic cerebral autoregulation Med. Eng. Phys 36 576–84 [PubMed: 24113077]

Panerai RB, Dawson SL and Potter JF 1999 Linear and nonlinear analysis of human dynamic cerebral autoregulation Am. J. Physiol. Heart Circ. Physiol 277 H1089–99

Petersen NH, Silverman A, Wang A, Kodali S and ShethK N 2019 Association of personalized blood pressure targets with hemorrhagic transformation and functional outcome after endovascular stroke therapy JAMA Neurol 76 1256–8 [PubMed: 31355872]

Raissi M, Perdikaris P and Karniadakis 2019 Physics-informed neural networks: a deep learning framework for solving forward and inverse problems involving nonlinear partial differential equations J. Comput. Phys 378 686–707

Rangel-Castilla L, Gasco J, Nauta HJW and Okonkwo DO 2008 Cerebral pressure autoregulation in traumatic brain injury Neurosurgical Focus 25 E7

Reinhard M, Muller T, Timmer J and Hetzel A 2003b Transfer function analysis for clinical evaluation of dynamic cerebral autoregulation-a comparison between spontaneous and respiratory-induced oscillations Physiol. Meas 24 27–43 [PubMed: 12636185]

Reinhard M, Roth M, Muller T, Czosnyka M, Timmer J and Hetzel A 2003a Cerebral autoregulation in carotid artery occlusive disease assessed from spontaneous blood pressure fluctuations by the correlation coefficient index Stroke 34 2138–44 [PubMed: 12920261]

Roweis ST and Saul LK 2000 Nonlinear dimensionality reduction by locally linear embedding Science 290 2323–6 [PubMed: 11125150]

Schetzen M 2006 The Volterra and Wiener Theories of Nonlinear Systems (Malabar, Florida: Krieger Pub.)

Singer A, Erban R, Kevrekidis IG and Coifman RR 2009 Detecting intrinsic slow variables in stochastic dynamical systems by anisotropic diffusion maps Proc. Natl. Acad. Sci 106 16090–5 [PubMed: 19706457]

Tan C 2012 Defining the characteristics relationship between arterial pressure and cerebral flow J. Appl. Physiol 113 1194–200 [PubMed: 22961266]

Tarumi T, Dunsky DI, Khan MA, Liu J, Hill C, Armstrong K, Martin-Cook K, Cullum CM and Zhang R 2014 Dynamic cerebral autoregulation and tissue oxygenation in amnestic mild cognitive impairment J. Alzheimers Dis 41 765–78 [PubMed: 24670396]

Tenenbaum JB, Silva VD and Langford JC 2000 A global geometric framework for nonlinear dimensionality reduction Science 290 2319–23 [PubMed: 11125149]

Tian F, Tarumi T, Liu H, Zhang R and Chalak L 2016 Wavelet coherence analysis of dynamic cerebral autoregulation in neonatal hypoxic-ischemic encephalopathy Neuroimage Clin. 11 124–32 [PubMed: 26937380]

Trajman A and Luiz R 2008 Mcnemar chi2 test revisited: comparing sensitivity and specificity of diagnostic examinations Scand J. Clin. Lab Invest 68 77–80 [PubMed: 18224558]

Vlachas PR, Byeon W, Wan ZY, Sapsis TP and Koumoutsakos P 2018 Data-driven forecasting of high-dimensional chaotic systems with long-short term memory networks Proc. R. Soc. A A474 20170844

Zhu Y, Zabaras N, Koutsourelakis PS and Perdikaris P 2019 Physics-constrained deep learning for high-dimensional surrogate modeling and uncertainty quantification without labeled data J. Comput. Phys 394 56–81

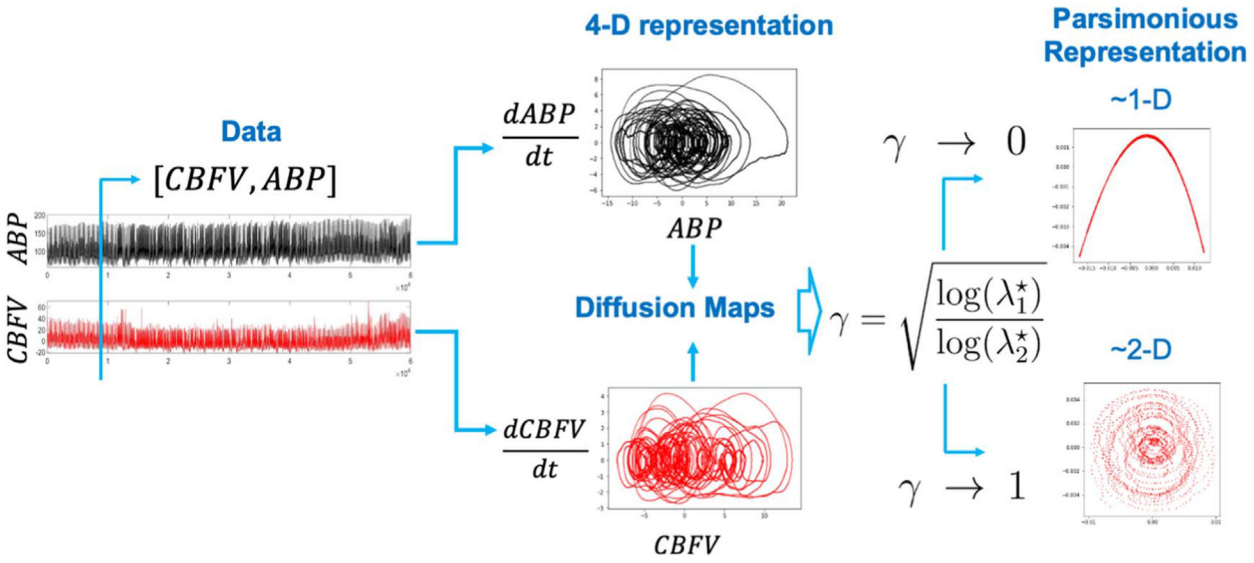

Figure 1.

Mechanization of the proposed technique based on diffusion maps for parsimonious modeling and analysis of DCA.

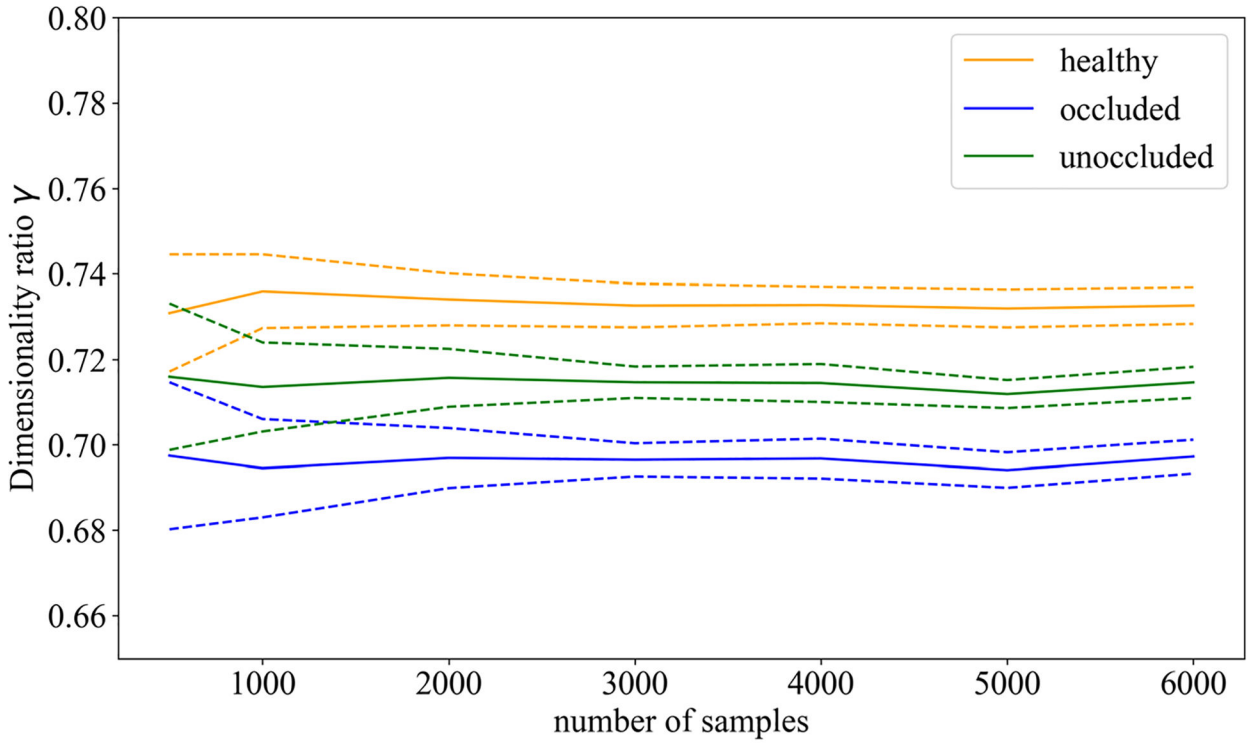

Figure 2.
Dimensionality ratio γ estimates based on various numbers of sample points.

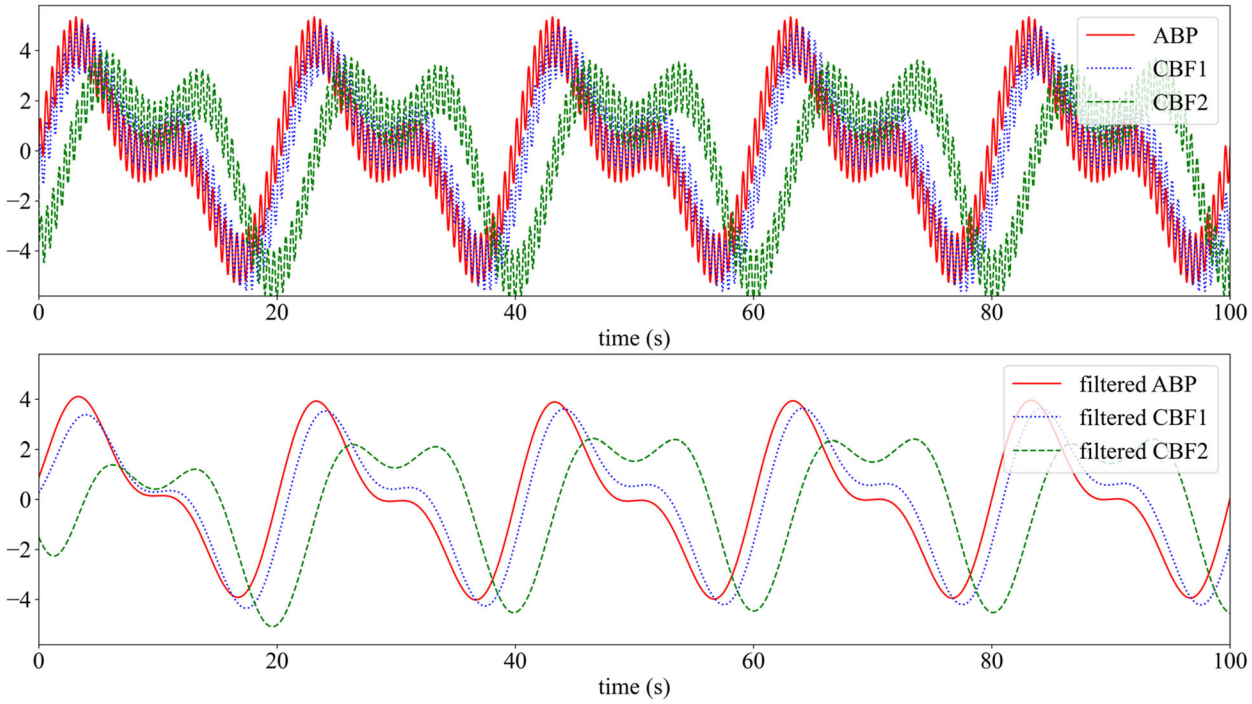

Figure 3.
Synthetic ABP and CBF signals before and after filtering for the first 100*s*.

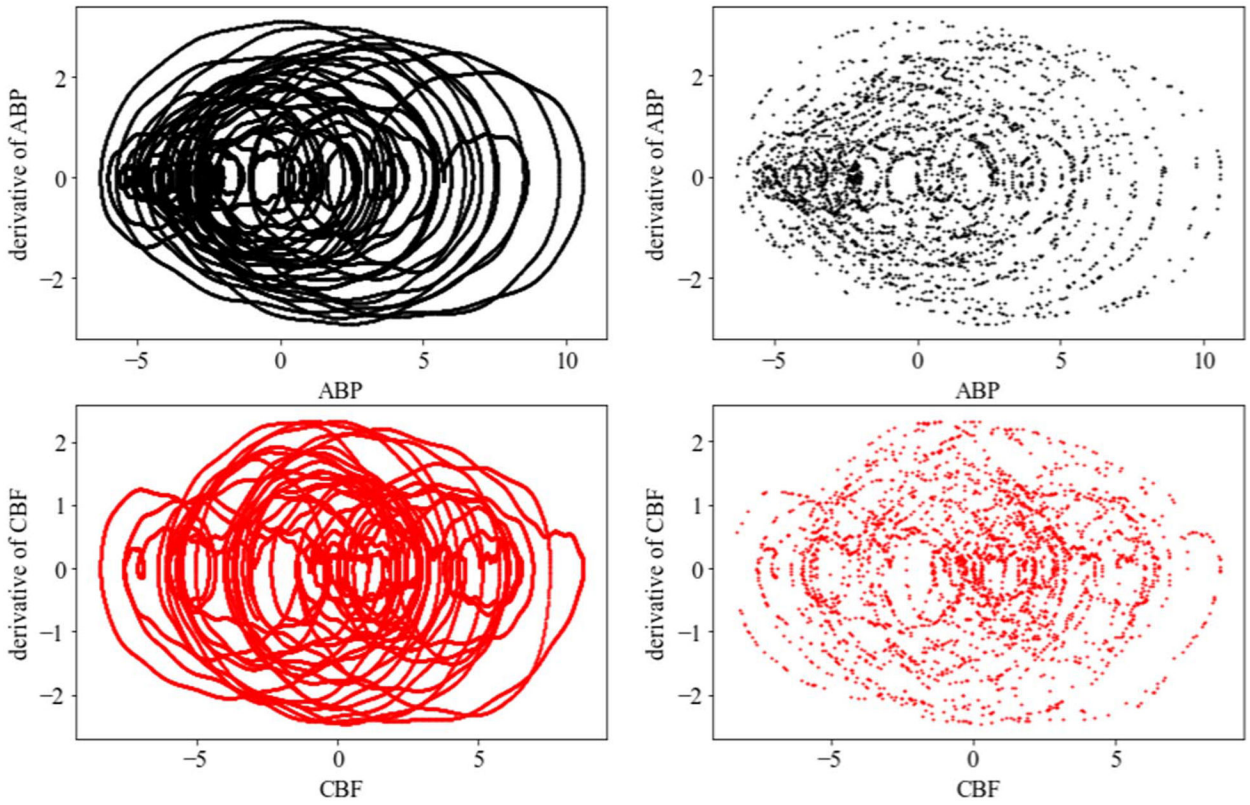

Figure 4.
Indicative ABP-CBFV time-history: 3000 samples randomly selected (right) out of the 55 000 points (left).

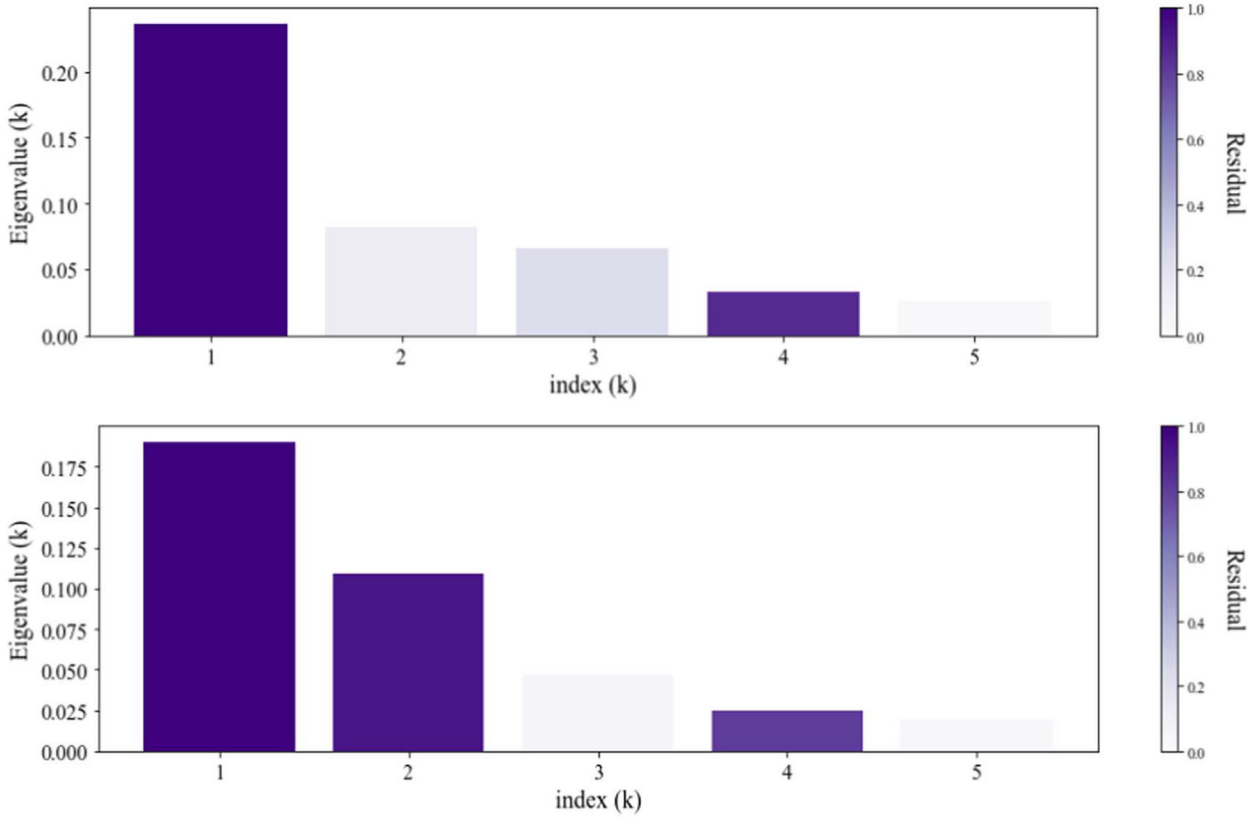

Figure 5.

Computed eigenvalues λ_k and their residuals r_k corresponding to the two sides of an ICA patient: occluded side with a ratio $\gamma = \sqrt{\frac{\log(\lambda_1^*)}{\log(\lambda_2^*)}} = \sqrt{\frac{\log(0.25)}{\log(0.04)}} = 0.65$ (top); unoccluded side with a ratio $\gamma = \sqrt{\frac{\log(\lambda_1^*)}{\log(\lambda_2^*)}} = \sqrt{\frac{\log(0.18)}{\log(0.10)}} = 0.86$ (bottom).

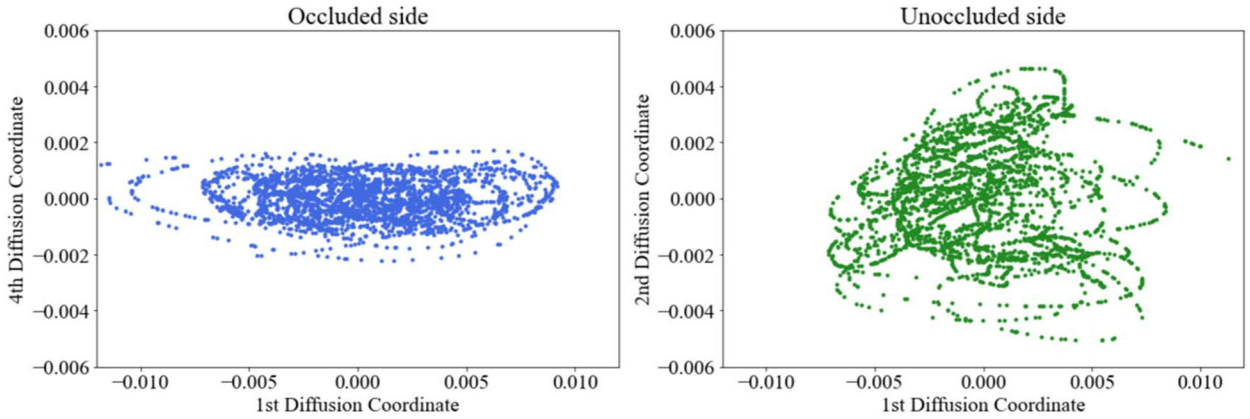

Figure 6.

Diffusion coordinates $\lambda_k^{\star} \cdot \psi_k(i)$ corresponding to the two sides; In the occluded side (left), a smaller γ value ($\gamma = 0.65$) relates to lower-dimensional, hypoactive, dynamics (impaired DCA), whereas in the unoccluded side (right), a larger γ value ($\gamma = 0.86$) relates to higher-dimensional, active, dynamics (healthy DCA).

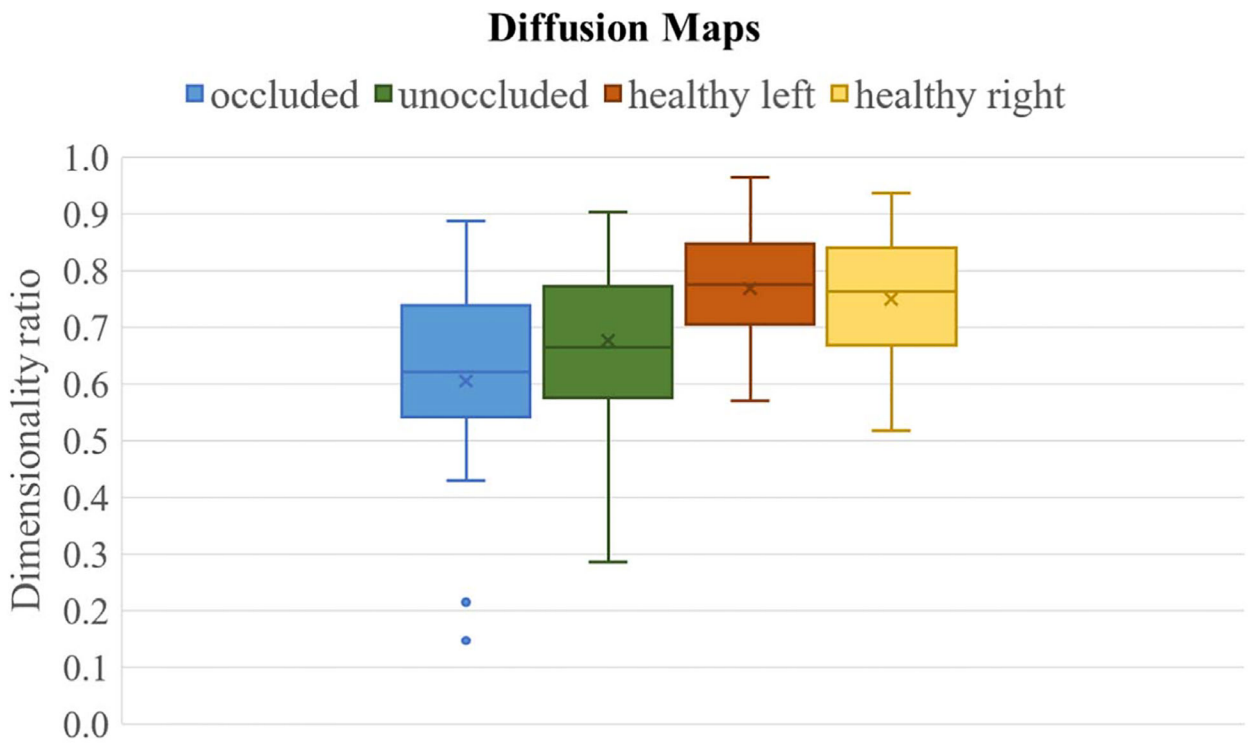

Figure 7.
Box plots of dimensionality ratios γ.

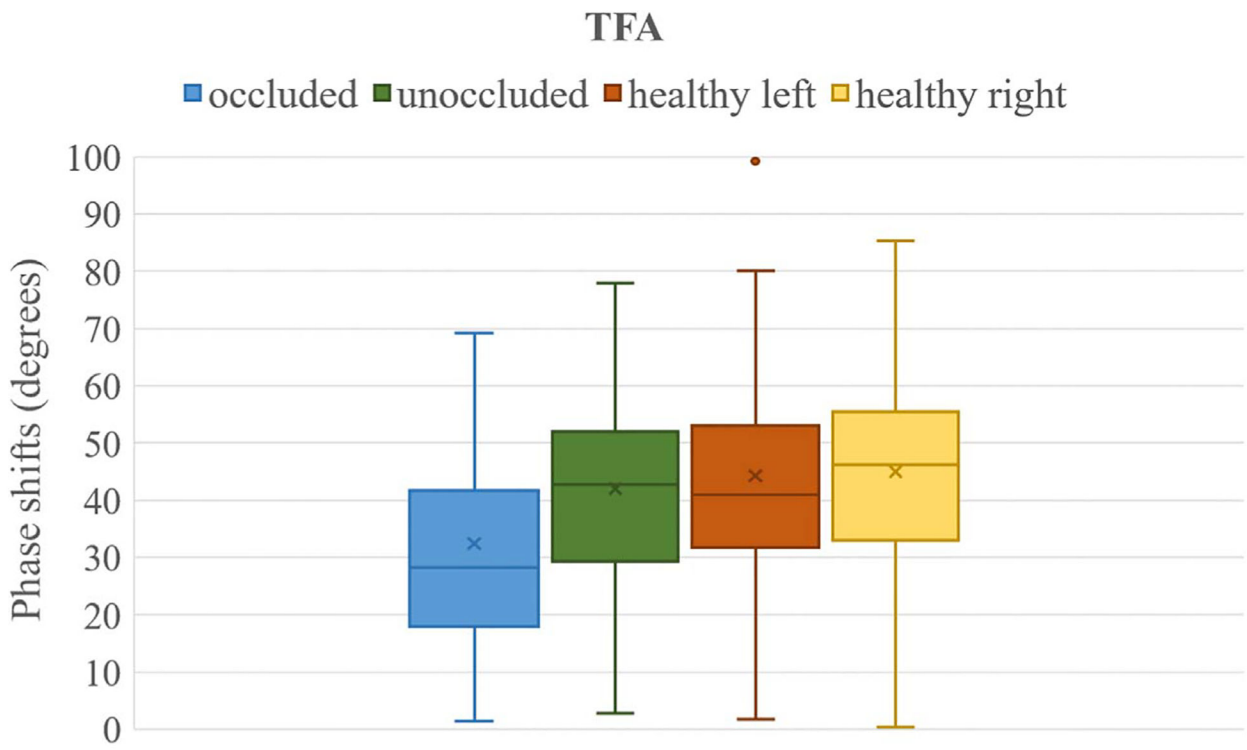

Figure 8.
Box plots of phase shifts based on standard TFA.

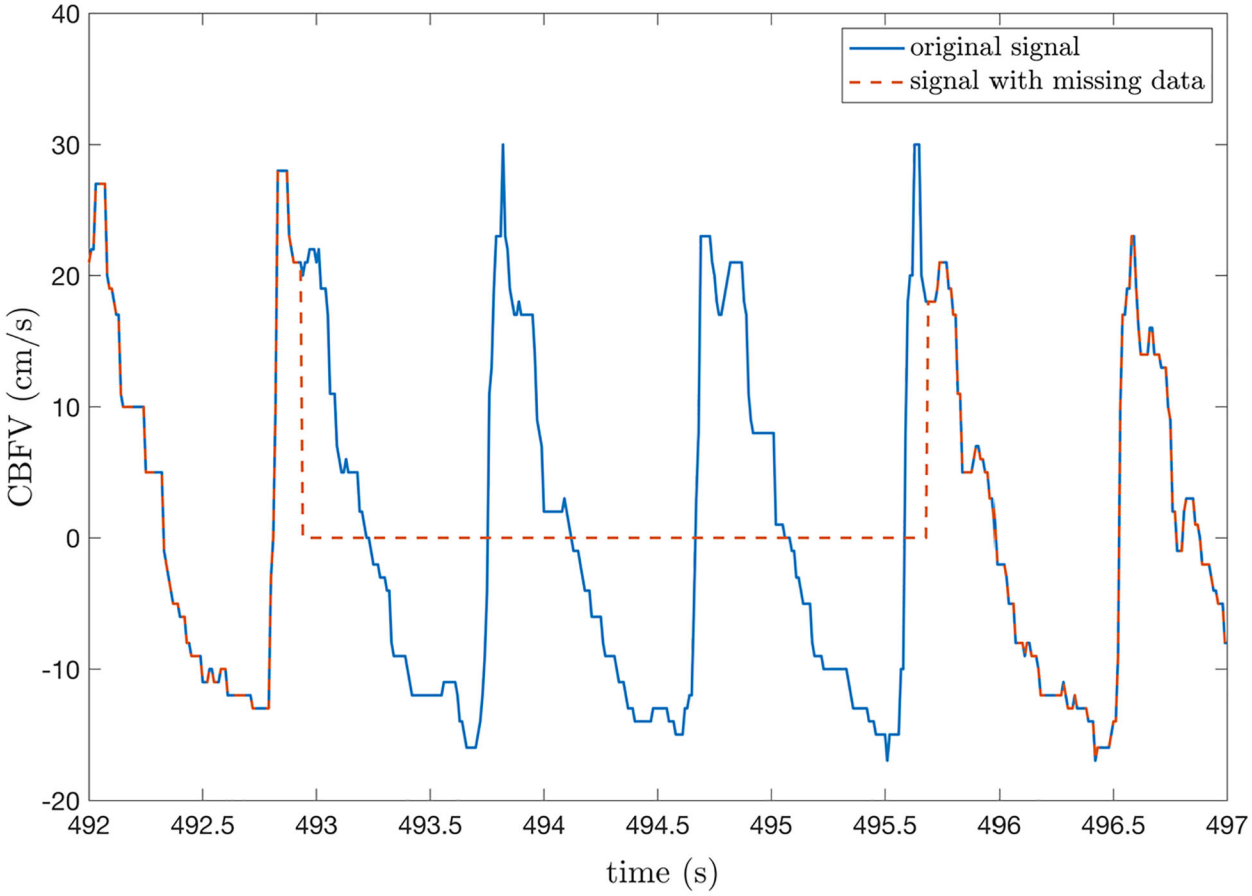

Figure 9.
Demonstration of missing data in the CBFV signal.

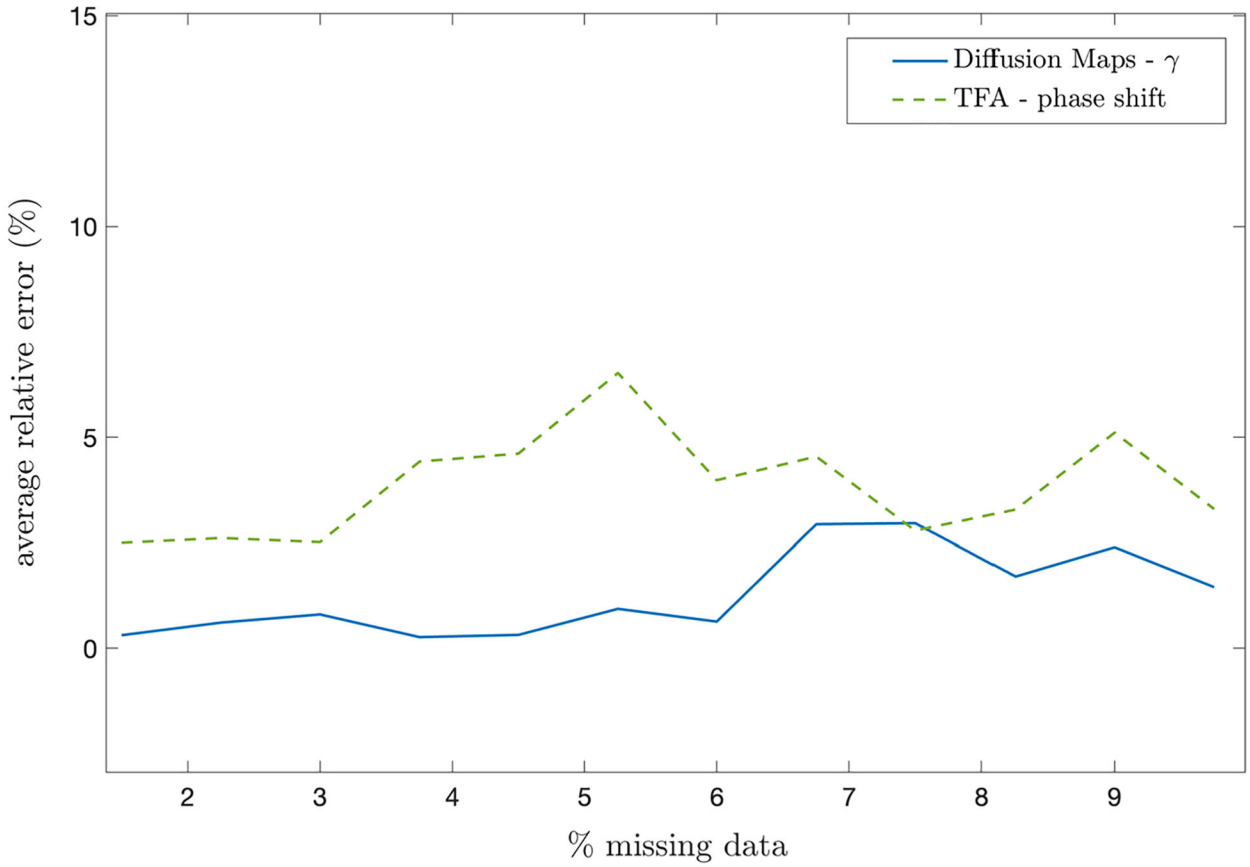

Figure 10.
Average relative errors referring to diffusion maps- and TFA-based biomarkers due to the presence of incomplete data in CBFV signals.

Table 1.

Diffusion maps-based statistical analysis of γ referring to carotid stenosis or occlusion patients and to healthy volunteers.

Sides	Occluded/stenotic	Unoccluded	Healthy left	Healthy right
Number of subjects	31		46	
Median (γ)	0.62	0.66	0.78	0.76
(IQR)	(0.54–0.74)	(0.58–0.77)	(0.71–0.84)	(0.67–0.83)
		p-values		
Two sides	0.05		0.47	
ICA occlusion/stenosis versus healthy group	10^{-5}		—	
Occluded/stenotic versus healthy group	10^{-5}	—	—	
Unoccluded versus healthy group	—	0.005	—	

Table 2.

TFA-based statistical analysis of phase shifts referring to carotid stenosis or occlusion patients and to healthy volunteers.

Sides	Occluded/ stenotic	Unoccluded	Healthyleft	Healthy right
Number of subjects	31		46	
Median (degrees)	28.8	42.7	41	46.3
(IQR)	(19.5–42.9)	(30.6–50.8)	(31.8–52.8)	(33.6–55.2)
		p-values		
Two sides	0.03		0.61	
ICA occlusion/stenosis versus healthy group	0.01		—	
Occluded/stenotic versus healthy group	$4 \cdot 10^{-3}$	—	—	
Unoccluded versus healthy group	—	0.59	—	